Nigussie Melessew (Orcid ID: 0000-0001-7827-5117)
Moldwin Mark, B. (Orcid ID: 0000-0003-0954-1770)
Radicella Sandro (Orcid ID: 0000-0002-1907-3715)
Yizengaw Endawoke (Orcid ID: 0000-0001-5772-3355)
Zou Shasha (Orcid ID: 0000-0001-7726-2349)
Nava Bruno (Orcid ID: 0000-0002-5240-9137)

The effect of F-layer zonal neutral wind on the monthly and longitudinal variability of equatorial ionosphere irregularity and drift velocity

Melessew Nigussie[1], Mark B. Moldwin[2], Sandro Radicella[3], Endawoke Yizengaw[4], Shasha Zou[2], Bruno Nava[3]

[1]WasheraGeospace and Radar Science Research Laboratory, Bahir Dar University, Ethiopia

[2]Climate and Space Sciences and Engineering, University of Michigan, USA

[3]Telecommunication/ICT for Development Laboratory, the Abdus Salam International Center for Theotretical Physics, Trieste, Italy

[4]Space Science Department, the Aerospace Corporation, El Segundo, USA

Abstract

The effect of eastward zonal wind speed (EZWS) on vertical drift velocity (**E**x**B** drift) that mainly controls the equatorial ionospheric irregularities has been explained theoretically and through numerical models. However, its effect on the seasonal and longitudinal variations of **E**x**B** and the accompanying irregularities has not yet been investigated experimentally due to lack of F-layer wind speed measurements. Observations of EZWS from GOCE and ion density and **E**x**B** from C/NOFS satellites for years 2011 and 2012 during quite times are used in this study. Monthly and longitudinal variations of the irregularity occurrence, **E**x**B**, and EZWS show similar patterns. We find at most 50.85% of longitudinal variation of **E**x**B** can be explained by the longitudinal variability of EZWS only. When the EZWS exceeds 150 m/s, the longitudinal variation of EZWS, geomagnetic field strength, and Pedersen conductivity explain 56.40-69.20% of the longitudinal variation of **E**x**B**. In Atlantic, Africa, and Indian sectors, from 42.63% to 79.80% of the monthly variations of the **E**x**B** can be explained by the monthly variations of EZWS only. It is found also that EZWS and **E**x**B** may be linearly correlated during Fall equinox and December solstice. The peak occurrence of irregularity in the Atlantic sector during November and December is due to the combined effect of large wind speed, solar terminator-geomagnetic field alignment, and small

This is the author manuscript accepted for publication and has undergone full peer review but has not been through the copyediting, typesetting, pagination and proofreading process, which may lead to differences between this version and the Version of Record. Please cite this article as doi: 10.1029/2019JA027671

geomagnetic field strength and Pedersen conductivity. Moreover, during June solstices small EZWS corresponds to vertically downward **E**x**B** which suggests that other factors dominate the **E**x**B drift** rather than the EZWS during these periods.

Corresponding author: Melessew Nigussie (melessewnigussie@yahoo.com)

Keywords: Equatorial ionospheric irregularities, vertical drift velocity, zonal neutral wind speed, C/NOFS, GOCE, longitudinal variation of ionospheric irregularity

1. **Background of the study**

The equatorial ionosphere exhibits unique features such as Equatorial Ionization Anomaly (EIA), Equatorial Spread F (ESF) and Equatorial Plasma Bubbles (EPB), among others. ESF is the generic name given to irregularities of the equatorial ionospheric electron density in the post-sunset period (Booker and Walls, 1938). Post-sunset enhancement of zonal electric field at the magnetic equator, usually called the Pre-reversal enhancement (PRE), is the main factor for the generation of ESF (Farley et al., 1986; Fejer et al., 1979, 1999). The evening time equatorial ionosphere is uplifted to a higher altitude through the enhancement of **E**x**B** vertical drift velocity, while the lower part is being decayed due to recombination (Anderson and Haerendel, 1979). This may create a situation that the Rayleigh-Taylor Instability (RTI) mechanism facilitates the growth of local perturbations in the bottom-side of the F-layer that evolves into ESF (Ott, 1978; Sultan 1996).

The seasonal and longitudinal variations of ESF have been studied using models and experimental data. The seasonal maximum occurrence of irregularities, in a given longitude**,** is found to correlate well with the times of the year when the solar terminator and geomagnetic field lines become nearly parallel (Tsunoda, 1985). Near the solar terminator the Earth's ionosphere crosses into the dark side of the Earth while the E region conductivity decays that causes the enhancement of the downward electric field and the F region ionosphere drifts strongly eastward. Ultimately, the increase in downward electric field creates a corresponding enhanced eastward electric field and upward drift of plasma. The rate of the decay of field-line conductivity of the ionosphere at the E region north and south of the dip equator is determined by the alignment or mis-alignment of the magnetic meridian and the solar terminator. When the two conjugate E regions cross the solar terminator simultaneously, there is a rapid increase in the downward directed E field

causing a larger PRE magnitude. When the two conjugate E regions cross the solar terminator at different times, the increase in the downward directed E field is slower, which limits the PRE magnitude (Rishibeth, 1971; Eccles et al., 2015). The growth rate of irregularity and vertical drift velocity have direct relation. In addition, the vertical drift velocity is inversely related to the geomagnetic field strength; indicating that as the geomagnetic field strength decreases the vertical drift velocity increases (Ren et al., 2009). This implies that the solar terminator and geomagnetic field alignment and low equatorial geomagnetic field strength can enhance the growth rate of irregularities. However, there is no clear explanation for the maximum occurrence of irregularities that appear during June Solstice (in Africa) apart from speculation by Tsunoda, (2010); he/she proposed that within the inter-tropical convergence zone (ITCZ) near the geomagnetic dip equator due to mesoscale convective system in the troposphere, atmospheric gravity waves can be generated and propagate upward and dissipate energy that in turn creates seed perturbation that together with RTI-growth rate could produce the observed ionosphere irregularities in June solstices in Africa sector. Similarly, quite a number of observational studies on the seasonal and longitudinal variations of the ESF have been done using observations (Kil and Heelis 1998; Burke et al., 2004a; Burke et al., 2004b; Huang et al. 2001, Hei et al., 2005; Su et al., 2006). Hei et al. (2005), using AE-E satellite data, reported the maximum occurrence is observed in West Africa and the West Pacific. They also show that peaks of irregularity occurrence in these regions migrate eastward from February through October; in winter months (November, December, and January) the Pacific peak disappears while the African peak is shifted to the west. Conversely, they observe year-round minimal occurrence of irregularities in the West South America (240-300^{o}E) and Indonesia/Indochina (90-120^{o}E) sectors. Similarly, other studies showed the highest and lowest occurrence of irregularities in the Atlantic-Africa and India-Pacific sectors, respectively (Burke et al. 2004a, 2004b; Kil and Heelis, 1998; Huang et al., 2001). In addition, Su et al. (2006), using ROCSAT (Republic of China Satellite) observations, showed that the highest occurrence of irregularities moved from around 0^{o} in March equinox to 30^{o}E in June solstices and then moved back to 20^{o}E in September and moved further to -30^{o}E in December solstices. Longitudinal variations of the occurrence of ESF have been explained by the longitudinal variations of different factors such as PRE (or vertical drift velocity), equatorial geomagnetic field strength, magnetic declination, and geographic locations of the dip equator (e.g., Burke et al., 2004a; Vichare and

Richmond, 2005; Zhang et al., 2012). Huang and Hairston (2015) have shown that the high occurrence of irregularities between 240 and 360°E longitudes during Equinox and December solstices correlates with the large post-sunset vertically upward drift velocity; they also showed that the low occurrence of irregularities correspond well with post-sunset small or downward drift velocities around ±60° longitude during June solstices. Su et al. (2006) also found high occurrence of ESF for the regions with upward vertical drift velocity after sunset. The low occurrence of irregularities in the India-Pacific sector is explained by the smaller vertical drift velocity due to strong equatorial magnetic field strength in the region, which produces smaller growth rate of RTI compared to other sectors (Huang et al., 2001; Burke et al., 2004a). The low occurrence of irregularities in the eastern Pacific or West Coast of South America has been explained by the reduction of RTI growth rate due to enhancement of E layer Pedersen conductance by precipitating radiation belt particles (Burke, et al., 2004a, b). The highest occurrence of ESF between South America and Atlantic sectors (-60 to 0°) is explained by the effect of strong growth rate of RTI due to solar terminator-geomagnetic field line alignment and lower equatorial geomagnetic field strength (Burke et al., 2004a; Su et al., 2006). The alignment between the solar terminator and geomagnetic field lines enhances the longitudinal gradient of E-layer integrated Pedersen conductivity that in turn increases the vertical drift velocity (Tsunoda, 1985) and growth rate of irregularities. However, the solar-terminator-geomagnetic field alignment is unable to explain the high occurrence of irregularities in the African sector during June solstices.

None of the above studies on ESF occurrence rates explore the relationship of longitudinal variation of thermospheric zonal neutral winds in F region and the longitudinal variation of occurrence of irregularities due to the lack of observations of zonal neutral wind speed in the post-sunset period (Yizengaw et al., 2013). Theoretical investigations give more emphasis to the role of thermospheric zonal neutral wind on the generation of PRE that mainly controls the generation of irregularities (Farley et al., 1986; Eccles et al., 2015; Richmond and Maute, 2014; Maute et al., 2012). Maute et al. (2012) have shown, using the TIME-GCM simulations, that the evening F-region wind is more important than the E region wind in controlling the magnitude of vertical drift velocity and its longitudinal variations of equatorial ionosphere. This motivates our study to complement and substantiate those theoretical investigations using ionospheric observations. In this study, in-situ observations of F-region zonal neutral wind speed, ion density, and vertical plasma

drift velocity during PRE hours, from GOCE and C/NOFS satellites will be presented; linear correlations between longitudinal variations of magnitude of vertical plasma drift velocity and zonal neutral wind speed during PRE hours will be determined; also multiple linear regression techniques will be applied to develop an empirical model for magnitude of vertical plasma drift velocity during PRE hours as a function of zonal neutral wind speed, magnetic field strength, and integrated Pedersen conductivity.

2. **Data and analysis procedure**

2.1 **Data**

The GOCE satellite was launched in 2009 to retrieve information of the Earth's static gravity field at high spatial resolution (Doornbos et al., 2013 and the references therein). It was a polar orbiting satellite with orbital inclination of about 97^{o} and orbital altitude from about 220 to 280 km. Applying different techniques (Doornbos et al., 2013), thermospheric neutral density and wind speed have been estimated with 10 second sampling rate (Liu et al., 2016 and the references therein) at the altitudes from 220 to 280 km. These data, from 2009 to 2013, are available for public use. The region of the ionosphere-thermosphere system that has been monitored by GOCE is the bottom side of the ionospheric F layer where ionospheric irregularities are believed to be initiated (Sultan, 1996) by the RTI mechanism. Similarly, the C/NOFS satellite was developed to understand, model, and forecast the Earth's equatorial ionospheric irregularities (de La Beaujardiere et al., 2004). C/NOFS was launched in 2008 (and was operational until 2015) and had an elliptical orbit at altitudes from 400 to 850 km, with orbital period of 96 minutes and inclination of 13^{o}. The instruments on-board C/NOFS include the Ion Velocity Meter (IVM) to measure the ion density and velocity (de La Beaujardiere et al., 2004). C/NOFS data are available for public use, too. Ionosphere-thermosphere system observations such as zonal wind speed from GOCE and ion density and vertical drift velocity from C/NOFS obtained in the low latitude ionosphere are used in this study. A large number GOCE and C/NOFS conjugate passes are identified in 2011 and 2012 during quiet days ($Ap < 15$).

2.2 Analysis procedure

Different methods have been used as indicator of ion density irregularity occurrence. For instance, Huang et al. (2014, 2015) have shown that the standard deviation of residuals for every 10

second observation from the 60 second means is a good indicator for perturbations of ion density. A similar technique is applied in this study, but the mean is taken from every 10 second observation and mathematically ion density perturbation is given by

$$\delta N = \left(\frac{1}{n} \sum_{i=1}^{n} (N_i - N_m)^2 \right)^{\frac{1}{2}}, \qquad (1)$$

where n equals 10 and N_i and N_m are ion density observation every second and their 10-second mean, respectively**.** Huang et al. (2014) and the references therein indicated that the ion density perturbation, δN greater than 10^{10} ions per m^3 is taken as signatures of ionospheric irregularities. Ion density perturbation is computed using C/NOFS observations obtained within $\pm 15^o$ latitude from the magnetic equator for each orbit and at an apex heights from 400 to 800 km. Daily ion density perturbations are computed from all orbits of C/NOFS in a day (i.e. about 16 orbits per day). Irregularity occurrence probability maps are produced by taking average value of perturbations obtained in the days of a month for different longitude bins. To get an understanding of the association between drift velocity and irregularity occurrence, maps of maximum value of vertical drift velocity observations between 1800 to 1900 LT are developed and compared with the maps of irregularity occurrence. Ion density irregularities corotate with the Earth and zonally drift from one longitude sector to the other before decaying (Huang and Hairston, 2015). This means the same region of irregularities has a possibility to be observed more than once by C/NOFS. This can create ambiguity in associating the cause and effect relationship between ionospheric irregularity and vertical drift velocity due to PRE. To minimize this kind of issue, Huang et al. (2015) considered only ion density observations in an orbit of C/NOFS during 1900 to 2100 LT and this procedure is adopted in this study. Monthly maximum vertical drift velocity maps are produced by collecting the maximum value of the drift velocity from each orbit in the month.

Occurrence maps of ion density perturbation and drift velocity using observations from C/NOFS and other satellites have been done before (Huang and Hairston, 2015; Kil et al., 2009). The main emphasis of this study is to see the relationship between the occurrence of irregularities in relation with drift velocity and zonal neutral wind speed. GOCE monitored the ionosphere-thermosphere system every day in the years 2009 and 2013. It had about sixteen full orbits in a day. The zonal neutral wind speed observed by this satellite within $\pm 3^o$ from the magnetic equator and between 1800 and 1900 LT is collected from each orbit for every day and then the mean zonal wind

speed is computed for each orbit. This mean zonal wind speed is calculated just at the magnetic equator over the globe**.** Monthly values of zonal wind speed as a function of longitude are computed for the same longitude bins as used to compute maps of ion density irregularity occurrence and drift velocity.

3. **Results**

Applying the procedures described above, analysis results of ion density irregularities, vertical drift velocity and zonal neutral wind speed are presented in this section. Figure 1 shows sample results of ion density irregularities (top row**),** drift velocity (middle row) and zonal neutral wind speed (bottom row) for 16, 17 November 2011, 16 and 17 November 2012, respectively. The longitudinal variation plots of ion density perturbations and maximum drift velocities are obtained from the entire orbits of C/NOFS for each day. Each dot in the drift velocity panel represents maximum value of drift velocities obtained between 1800 and 1900 LT from a single orbit of C/NOFS. In the bottom panels, each vertically tilted color-coded line shows the zonal neutral wind speed corresponding to each orbit of GOCE within 1800 to 1900 LT versus longitude and latitude. The geographic latitude and longitude locations of the magnetic equator (magenta dotted line) and $\pm 3^{o}$ from the magnetic equator are presented in these panels. The deep yellow color indicates the highest zonal wind speed while the deep blue represents the smallest speed. As can be seen in the top panels, the ion density perturbations show apparent longitudinal variations. Strong ion density perturbations are obtained for the longitudes from about -50^{o} to 80^{o} whereas weak perturbations are found in the other longitudes during these days. Similarly, maximum vertical drift velocities, in the longitudes from -50^{o} to 80^{o} for each day, are relatively higher than those obtained in the other longitudinal sectors. There is clear correspondence between maximum drift velocities and maximum zonal wind speeds, for example see on 17 November 2012**;** however, the correspondence shown in 2012 is better than that of 2011. This is an indication of the good correlation among maximum occurrence probability of ion density perturbations, vertical drift velocity, and zonal wind speed.

Figures 2 and 3 show the distribution of average zonal neutral wind speeds at 18-19 LT, which are obtained for each pass between ±3 degree latitude from the dip equator, for each month in the years 2011 and 2012, respectively; the individual mean zonal speeds represent zonal speeds at

the dip equator over the globe for every 3-degree longitude bin. As seen the minimum and maximum mean zonal wind speeds are obtained in June and December solstices months, respectively; specifically, in 2011 the minimum and maximum mean values are 68 m/s (June) and 172 m/s (in November). Similarly, in 2012 the minimum and maximum mean values are 93 m/s (June) and 168 m/s (in October). In both years, the mean zonal wind speed above 150 m/s are obtained in the months of October, November, and December. The standard deviations of zonal neutral wind speeds are obtained for each month of both years in the range from 19-29 m/s (see each panel of Figures 2 and 3).

Figure 4 shows the variations of the irregularity occurrence rates (first and second panel columns, from the left), the average of the maximum ion drifts (third panel column), and the average of the zonal wind speed (fourth panel column) with respect to longitude and months for the years 2011 (top panels) and 2012 (bottom panels). The first two columns, from the left, show the occurrence probability of ion density perturbations for two threshold values: $\delta N > 1\times10^{10}$ ions per $m^3$and $\delta N > 2.5\times10^{10}$ ions per m^3, respectively. The monthly values of occurrence probability of ion density irregularities are computed by counting irregularities exceeding the threshold values within 10^o longitude bins, whereas the drift velocity and zonal wind speed maps are obtained by averaging in the same set of longitude bins (see 3^{rd} and 4^{th} columns of Figure 4). The irregularity occurrence probability maps show clear monthly and longitudinal variations in both years. To see the longitudinal variations, the globe is divided into five regions: the American sector (-140 to -70^oE), Atlantic sector (-70 to 0^oE), African sector (0 to 45^oE), Indian sector (45 to 105^oE), and Pacific sector (105 to -140^oE). These longitudinal sectors are indicated by the vertical dashed lines in Figure 4. As seen in the results of the year 2011 (top panel Figure 4), during October and April the occurrence probabilities of irregularity are higher in almost all longitudes as compared to other months; in addition, the occurrence probabilities during October are larger than that during April in all longitudes. This is in agreement with the previously reported seasonal asymmetry of irregularity and scintillations occurrences (Burke et al., 2004a; Paznukhov et al., 2012).

In the longitudes between -70^o and 0^o (Atlantic sector), the irregularity occurrence during December and November are very high and they are comparable to the peak occurrence during October in these longitudinal sectors. Similarly, in this longitudinal sector the occurrence probability of ion density irregularity is noticeable during January, February, and March; however,

the occurrence probability is smaller than the one obtained during October, November, and December. The smallest occurrence probability of irregularity is obtained during May to September in all longitudes except some parts of Africa during June and September. This is similar to the results obtained by Hei et al. (2005) using the AE-E satellite data. Similarly, the smallest occurrence probability is obtained during January, February, March, November, and December in all longitudes except in East America and Atlantic sectors.

The irregularity occurrence probability in the year 2012 shows slight differences with the one obtained in the year 2011. For the threshold of 1×10^{10} ion per m^3 irregularity, more than 10% occurrence probability is observed during all equinoctial months in all longitudes and during November, December, and January within -70^o to 0^o longitudes. Similarly, in the African sector (i.e. 0^o to 45^o longitude) more than 10% occurrence probability is obtained during June solstices. Similar patterns of irregularity occurrence are shown in the maps with threshold of 2.5×10^{10} ion per m^3. For both thresholds for the year 2012, the highest occurrence of irregularities is obtained during October, November, December, and February in the Atlantic sector. The occurrence during February is higher than the one during March and April. Also, seasonal asymmetry is clearly observed with the highest occurrence during September equinox and December solstices.

The drift velocity and zonal wind speed maps show clear monthly and longitudinal variations in both years. The highest drift velocity is observed between -70^o and 45^o longitudes during October, November, and December followed by January, February, March and April. Smaller or downward drift velocities are obtained during June solstice months in all longitudes. Like that of irregularity occurrence, maximum vertical drift velocity shows seasonal asymmetry; the highest first appear during October, November, and December compared to drifts during January, February, March and April, especially in the year 2011. White color on the maps of drift velocity indicates missing data. Interestingly, the monthly and longitudinal variations of the zonal wind speed show similar patterns with maps of seasonal and longitudinal variations of drift velocity and the irregularity occurrence probability. The highest zonal wind speed occurs in the same months and longitudes as the highest drift velocity and the irregularity occurrence. Relatively noticeable occurrence probability during June solstices in the African sector shows corresponding to relatively high drift velocity values as compared to other longitudinal sectors. During October, November, and December for both years, the highest wind speed is observed in all longitudes except between about

-145^o to -95^o (American sector) in general. Similarly, smaller (below about 90 m/s) zonal wind speed is observed during June solstice in all longitudes except about -95^o to -65^o. Surprisingly, small zonal neutral wind speed (below around 90 m/s) corresponds to downward vertical drift velocity (see results for June solstice).

Figures 5 and 6 show scatter plots of the mean vertical drift velocities versus the mean zonal neutral wind speed within every 30^o longitude bin for each month for the years 2011 and 2012, respectively. These plots are useful to understand the effect of longitudinal variations of the zonal neutral wind speed on the longitudinal variations of vertical drift velocity. As can be seen in Figure 5 there is a negative correlation between the longitudinal variations of the vertical drift and the zonal wind speed during March, April, and September; whereas in Figure 6 the negative correlation is obtained only during March. The negative correlation of the vertical drift and the zonal neutral wind speed implies that the relationship is anti-correlated that is increasing wind speed correlated with decreasing vertical drift. This anti-correlation is mostly observed when the maximum zonal wind speed is less than 150 m/s; this indicates that other parameters may dominantly affect the variation of vertical drift velocity during those months**.** The correlations obtained for the months of the year 2011 (Figure 5) are different: small correlations (between 0.1 and 0.3) for January, June, and September; medium correlation (between 0.3 and 0.5) for February, March, April, May, July, and September; large correlation (between 0.5 and 1) for October, November and December; almost no correlation (between 0 and 0.1) for August. Similarly, correlations obtained between the longitudinal variations of vertical drift and zonal wind speed for the months of the year 2012 are different: small correlation for the months of January, February, April, and August; medium for May, June, July, and December; large for March and November; and almost no correlation in September and October. The coefficient of determinations (r^2) for each month is computed and presented in each panel of Figures 5 and 6. For the months that show large correlation, the coefficient of determinations varies from 32.55% to 50.85%**.** These values are obtained during October, November, and December in 2011 (Figure 5) and March and November in 2012 (Figure 6). This indicates that the longitudinal variation of the zonal neutral wind can explain, at most 50.85% of the longitudinal variation of PRE vertical drift velocity (see November in Figure 6). Also, in a significant portion of the year, the longitudinal variation of zonal neutral wind cannot be used to explain the longitudinal variation of vertical drift velocity. Through the ionospheric dynamo

at F layer, the east ward zonal neutral wind can create vertical ion current that finally produces downward polarized electric fields (Eccles, 1998). These polarized electric fields can map down to the E layer and generate westward Hall currents that diverge after a fraction of a second and induce eastward electric fields that in turn result in the pre-reversal enhancement vertical plasma drift (Farley et al., 1986; Eccles, 1998). The observed linear relationship shown between the PRE vertical plasma drift and the eastward zonal neutral wind might be due partly to this process.

Similarly, Figure 7 shows the scatter plots of longitudinal variations of the vertical drift velocity versus the zonal neutral wind speed for different seasons of both 2011 (top panels) and 2012 (bottom panels) years. Seasons are classified as September equinox (August, September, and October), March equinox (February, March, and April), June solstices (May, June, and July), and December solstices (November, December, and January). Positive correlation is obtained in all of the seasons in both years except March equinox in 2011. Large (>0.5) correlation is obtained for December solstices and September equinox in 2011; medium (>0.3 and 0.5 <) correlation for June solstices and September equinox for the year 2012; small (<0.3) correlation for March and June solstices in 2011 and December and March equinox in 2012. The coefficient of determination computed for these seasons indicate the longitudinal variations of zonal wind speed can explain at most 62.76% of the longitudinal variation of vertical drifts velocity in the 2011 September equinox.

As can be seen, for example, during March and November 2011 and 2012, the correlations between the longitudinal variations of drift velocity and zonal neutral wind speed are negative and positive (see Figures 5 and 6), respectively. The negative and small correlations imply that zonal neutral wind may not be the only factor for the longitudinal variations of the vertical drift velocity as it is indicated by different studies (Burke et al., 2004a; Vichare and Richmond, 2005). To compare the effect of geomagnetic field strength, eastward zonal neutral wind speed, and conductivity of the ionosphere on the longitudinal variations of vertical drift velocity, Figures 8 (for year 2011) and 9 (for year 2012) are produced corresponding to sample negative and positive correlations shown in Figures 5 and 6. The 1st, 2nd, 3rd, and 4th rows of Figures 8 and 9 show the longitudinal variations of vertical drift velocity, zonal neutral wind speed, and geomagnetic field strength at the magnetic equator, and field-line integrated Pedersen conductivity, respectively. The field-line integrated Pedersen conductivities are computed using collision frequency and Pedersen conductivity equations available in Shunk and Nagy (2009), IRI-2016 (International Reference

Ionosphere), NRLMSISE-00, and IGRF models. IRI-2016, NRLMSISE-00, and IGRF models have been used to compute ionospheric, thermospheric, and geomagnetic field parameters that have been used as input for Pedersen conductivity, collision frequency and gyro-frequency equations. Integration of Pedersen conductivity has been done along the geomagnetic field lines above 150 km from the surface of the Earth corresponding to 600 km apex height at 1900 LT. As seen in the bottom panels of Figures 8 and 9, the conductance varies from 5-41 mho and this is in agreement with the results obtained by Eccles et al. (2015) in general. The maximum conductance is obtained the American longitudinal sector. The drift velocities corresponding to negative correlations (left panels) are below 50 m/s in all longitudes, but the one shown for positive correlations is above 50 m/s within the longitudes from -80 to 60^o. The zonal neutral wind speeds, corresponding to negative correlation, do not show strong longitudinal variations that are between about 100 m/s and 150 m/s in all longitudes, but the one corresponding to positive correlation is found between about 150 m/s and 220 m/s almost in all longitudes and the peak value is observed in the Atlantic longitudinal sector. The longitudinal variations of the geomagnetic field strength at the magnetic equator (3^{rd} panels from the top) have similar patterns both for the negative and positive correlation cases. But it shows strong longitudinal variations; the smallest and highest values are shown in Atlantic and Pacific sectors, respectively. The Pedersen integrated conductivity shows clearly the inverse of the longitudinal variations of the geomagnetic field strength as expected when the E region contribution is small.

Figures 10 and 11 show scatter plots of monthly vertical drift velocity versus monthly zonal wind speed for the years 2011 and 2012, respectively. The monthly scatter plots are provided for different longitudinal sectors with 30^o longitude bin and this provides twelve longitudinal sectors over the globe. The correlation between the monthly variations of drift velocity and monthly zonal wind speed shows a clear longitudinal asymmetry. Smaller or even slightly negative correlations are found for the region from -180^o to -150^o longitudes (Pacific sector) and in the -150^o to -120^o and 150^o to 180^o longitude bins (Pacific sector). Interestingly, large correlations are obtained in wide longitudinal bins from -120^o to 150 both years 2011 and 2012. These longitudinal ranges represent East America, Atlantic, Africa, India, and West pacific sectors.

Of the longitudinal bins that have shown large correlations, coefficient of determination above 50% are obtained in the longitudes between -90^o to 120^o for the year 2011 and between -60^o

to 90^o for the year 2012 except within 0^o to 30^o longitudes corresponding to Atlantic, Africa, and Indian sectors.

In the Figures 5, 6, 7, 10 and 11 the correlations between the maximum PRE vertical drift velocity and the zonal neutral wind speed (U) are displayed while ignoring the relationship of other parameters with the vertical drift. However, as shown in Figures 8 and 9 and determined by different studies (e.g. Ren et al., 2009), the vertical plasma drift is related with other parameters, such as geomagnetic field (B) and field-line integrated Pederson conductivity ($\sum_p$) as well. Considering the effect of longitudinal variation of zonal neutral wind, the geomagnetic field strength and Pedersen conductivity on the longitudinal variations of the vertical drift are inseparable; their relationship with PRE vertical drift, applying multiple-linear regression, is obtained and results are shown in Table 1. The model used for multiple linear regression is

$$Vd = \beta_o + \beta_1 U(l) + \beta_2 B(l) + \beta_3 \Sigma_p(l), \quad (2)$$

where, V_d is the vertical drift velocity and β_o, β_1, β_2, and β_3 are model coefficients, l is longitude. As seen in this table when the neutral wind speed is very high (above 150 m/s) for the November 2011 and 2012, the zonal neutral wind speed coefficients are positive and these values are also significant (the calculated P-values are less than or equal to alpha values). For the months of November 2011 and 2012, these three parameters can describe 56.40% and 69.20% of the longitudinal variability of vertical drift velocity, respectively; whereas for the months of March 2011 and 2012, the association between vertical drift velocity and neutral wind speed is negative.

4. **Discussion**

The global distributions of the occurrence probability of ion density perturbation and the post-sunset maximum vertical drift velocity are derived from C/NOFS observations for the years 2011 and 2012 (Figure 4). Using the same data, Huang and Hairston (2015) derived yearly mean distribution of the occurrence probability of ion density perturbations and vertical drift maps for low (2008-2010) and high (2011-2014) solar activity years and found good correlation between the occurrence probability of irregularities and vertical drift velocity. The PRE vertical drift velocity, which has good correlation with the occurrence of irregularities (Huang and Hairston, 2015), depends on different physical parameters such as zonal neutral wind, geomagnetic field strength, conductivity of the ionosphere, and the angle between the solar terminator and geomagnetic field

lines (Burke, et al., 2004a; Vichare and Richmond, 2005). Theoretical studies have given more emphasis on the role of eastward zonal neutral wind speed on the generation of the PRE vertical drift velocity (Heelis, 2004; Heelis et al., 1974; Rishbeth, 1971; Farley et al., 1986; Eccles, et al., 2015). The objective of the current study is to investigate the effect of the longitudinal variations of the eastward zonal neutral wind speed, geomagnetic field strength, the Pedersen conductivity, and alignment between geomagnetic fields lines and solar terminator on the longitudinal variations of the PRE vertical drift velocity and the associated occurrence probability of the equatorial ionospheric irregularities to develop a more complete picture of the drivers of irregularities.

The monthly and longitudinal distributions of the occurrence probability of ion density perturbations obtained in the current study (see Figure 4) are consistent with previous studies using data from other satellites such as DMSP and ROCSAT-1 (Su, et al., 2006; Burke et al., 2004a; Gentile et al. 2006; Kil et al., 2009); with the highest occurrence probability in the Atlantic longitudinal sectors (-70 to 0^o longitude). Low occurrence probability of ion density perturbation is identified during June solstices in all longitudes expect in the African sector and this result is also consistent with earlier findings (Huang et al. 2013; Kil et al., 2013). The appearance of high occurrence of irregularities in all longitudes during the equinoctial months is also consistent with the results obtained by Hei et al. (2005) using AE-E satellite data. However, the occurrence probability of irregularities in September equinox is higher than that in March equinox almost in all longitudes; this is also in agreement with asymmetric occurrence probability of irregularity obtained in the American-Atlantic sectors using DMSP data (Burke et al., 2004a).The occurrence probabilities of irregularities maps and vertical drift maps (3^{rd} column in Figure 4) show similar monthly and longitudinal variations as it observed by previous studies (Kil et al., 2013; Huang and Hairston, 2015).

The highest occurrence probability of ion density perturbations, which is obtained in Atlantic longitudinal sectors (-70 to 0^o longitude), correlates with the highest magnitudes of the PRE vertical drift velocity and the eastward zonal neutral wind speed. Similarly, the lowest occurrence probability of irregularities obtained during May to June almost in all longitudes correlates with the smallest (or downward) vertical drift velocities and smallest (below around 90 m/s) eastward zonal neutral wind speed. In general, the zonal wind speed maps (4^{th} column in Figure 4) show similar monthly and longitudinal variations to the maps of the irregularity

occurrence and the vertical drift velocity, which is an interesting result. It is well established that the eastward zonal neutral wind at the F-layer drives vertically upward ion dynamo currents, which become divergence free after a fraction of a second and results vertically downward polarized electric fields (Heelis, 2004; Heelis et al., 1974; Rishbeth, 1971; Farley et al., 1986; Eccles et al., 2015**).** This vertically downward electric field is assumed to produce zonal electric field through two different mechanisms such as Curl-free mechanism and Hall current divergence mechanism (Eccles et al., 2015) and finally the PRE is superposition of enhanced zonal electric fields from these mechanisms. As it is explained via the Hall current divergence mechanism, mapping down to the E layer along the geomagnetic field, this electric field drives westward Hall currents that also become divergence free and results in zonal enhanced electric fields (or PRE) (Farley et al., 1986). Through Curl-free mechanism, Rishbeth (1971) also pointed out that the vertical downward polarized electric field get enhanced around sunset because of strong vertical gradient of conductivity due to the decay of ionization and high ion recombination rate at the E-layer while ionization still exist and recombination rate is weak at F-layer; at the sharp sunset edge of the F-layer dynamo, the enhanced vertically downward polarized electric field produces an edge effect that results zonal component electric field which is ultimately known as PRE. Simulation results have shown strong linkage between the zonal neutral wind and the PRE vertical drift velocity (Heelis, 2004; Maute et al., 2012; Eccles, et al., 2015). However, in the current study, it is clearly observed that in some longitudinal sectors (mostly between -70 and 0^{o} longitude) during June solstices, when the zonal wind speed is small, but still eastward, the vertical drift velocity can be downward. This may result from competition of the effect of PREs due to Curl-free mechanism and Hall current divergence mechanism; from numerical simulations, for both equinox and solstice, the magnitude of PRE due to curl-free mechanism dominates the one due to Hall current divergence mechanism but the peak values from these methods are more closer during solstices (Eccles et al., 2015). In addition, the peak value of PRE due to the Hall current divergence mechanism occur earlier than the corresponding value from Curl-free mechanism; also, vertical drift due to Hall current divergence mechanism directs downward after sunset whereas the one from Curl-free mechanism remains upward. Therefore, the downward vertical drift observed in this study while the zonal neutral wind speed directed to the east may be as a result of the dominance of downward vertical drift due to Hall current divergence mechanism over the Curl-free mechanism. In addition,

other factors may have role for the downward vertical drift; for example, quite time prompt penetration electric field and atmospheric gravity wave induced electric field may play a role for the downward directed vertical drift.

To investigate the relationship between the zonal neutral wind speed only and the vertical drift velocity, scatter plots of the vertical drift velocity versus the zonal neutral wind speed for each month (see Figures 5 and 6) and season (see Figure 7) are presented. The highest correlations obtained are 0.6501 (r^2~0.4226) and 0.7131 (r^2~0.5085) only during November 2011 and 2012 (see both Figures 5 and 6); the maximum 42.26% and 50.85% r^2 values found, for these months, indicate that 42.26% and 50.85% of the longitudinal variations of vertical drift velocity may be explained by the longitudinal variation of zonal neutral wind speed only. Since 92% (22 of 24) of the months studied have the coefficient of determinations below 42.26% and 50.85%, most of the time more than 50% of the longitudinal variations of the vertical drift velocity should be explained by the longitudinal variations of zonal neutral wind and other parameters, such as the geomagnetic field strength, the alignment between the geomagnetic field lines and solar terminator, and so on (Burke et al., 2004; Vichare and Richmond, 2005). As seen in Table 1, when the effects of the longitudinal variations of zonal neutral wind speed, geomagnetic field strength, and conductivity are considered on the longitudinal variations of PRE vertical drift velocity, the relationship increases; for November 2011 and 2012, 56.40% and 69.20% of the longitudinal variations of the PRE vertical drift can be explained by the longitudinal variations of those predictor variables. The remaining percentage of variability of PRE vertical drift velocity may be explained by other parameters variability like prompt penetrating and shielding electric fields, gravity wave induced electric fields, and so on. The linear regression results obtained also indicate linear relationship between the PRE vertical drift velocity and zonal neutral wind speed, which is consistent with theoretical investigations (Heelis, 2004; Eccles et al., 2015). This implies that this result complements previous theoretical findings done for understanding relationship between the zonal wind driven dynamo currents and the PRE vertical drift velocity.

Different factors are believed to affect the longitudinal variation of electric field and associated drift velocity; for example, the longitudinal variation of geomagnetic field strength, declination, and zonal neutral wind speed have contribution on the longitudinal variation of drift velocity as shown

in simulation studies (Vichare and Richmond, 2005; Ren et al., 2009). Above about 170km, both ions and electrons move together upward with the drift velocity,

$\boldsymbol{V}_d = \frac{\boldsymbol{E}x\boldsymbol{B}}{B^2}$, at the low latitude of the ionosphere (Rishbeth, 1971; Vichare and Richmond, 2005) where **E** is eastward zonal electric field and **B** is the horizontal geomagnetic field. This relation show that if the longitudinal variation of the zonal electric field is insignificant compared to the variation of geomagnetic field strength or if the zonal electric field is constant along the longitude, in region where the geomagnetic field strength is weaker, the vertical drift velocity will be higher (Huang et al., 2001; Vichare and Richmond, 2005; Ren et al., 2009); but in practice it is clear that both the neutral wind speed and geomagnetic field that can cause for the generation of the zonal electric field vary with longitude. Also, Heelis (2004) has shown that the vertically downward polarized electric field at the F layer due to ionosphere dynamo has a direct relationship with zonal neutral wind speed especially in the nighttime. This indicates in turn direct relationship between the vertical drift velocity and zonal neutral wind speed. The negative and positive correlations obtained during March and November 2011 and 2012 (Figures 8 and 9) may be due to the competition of the longitudinal variations of zonal neutral wind speed and geomagnetic field strength in affecting the longitudinal variations of the vertical drift velocity. The longitudinal variations of drift velocity, zonal neutral wind speed, geomagnetic field strength at the magnetic equator, and integrated Pedersen conductivity are shown in Figures 8 and 9 for March (left panels) and November (right panels) 2011 and 2012, respectively. In the left-hand side panels of Figures 8 and 9, the longitudinal variations of the drift velocity (top panels) does not follow the longitudinal variations of zonal neutral wind speed (2^{nd} rows from the top) instead it follows the inverse of the geomagnetic field strength. This may be due to relatively high longitudinal variation of geomagnetic field strength compared to the zonal electric field that can be generated by the zonal neutral wind speed (Eccles, et al., 2015) without much longitudinal variations. Conversely, as shown on the right-hand panels, the longitudinal variation of the drift velocity (top panels) does follow strongly the longitudinal variations of zonal neutral wind speed (2^{nd} rows from the top) instead of the geomagnetic field strengths. The zonal neutral wind speed in the right panels show clear difference with the one displayed in the left hand panels; the magnitude of zonal wind speeds shown in the right hand panels are stronger (U> 150 m/s in most of the longitudes) and show larger longitudinal variations than the one in the left hand side panels (U<150 m/s and almost constant at all longitudes). This

implies that strong eastward zonal neutral wind speed with considerable longitudinal variations may be the cause for strong electric field and vertical drift with similar longitudinal variations through ionosphere F-layer dynamo (Eccles, et al., 2015; Rishbeth, 1971) instead of the longitudinal variation of the geomagnetic field strength.

As pointed out by Farley et al. (1986), field aligned integrated conductivity has a strong effect on the field aligned coupling between the E and F layer electrodynamics. Integrated conductivities shown in these figures show clear inverse relation with the geomagnetic field strength; indicating the conductivity is strongly influenced by the Earth's magnetic field, which is in agreement with results shown by Vichare and Richmond (2005).

The enhanced drift velocities shown in Figures 4, 8, and 9 could be also complemented by the alignment between solar terminator and geomagnetic field lines (see Figure 12). Tsunoda (1985) suggested that during the months when the solar terminator is parallel with the geomagnetic field line, the drift velocity gets enhanced, which finally enhance the irregularity growth rate. This can be tested by correlating the strength of the drift velocity with difference of geomagnetic declination and solar terminator angles as described in Tsunoda's model (Burke at al., 2004) i.e $\alpha = \delta - \varepsilon$, where δ and ε are geomagnetic declination and solar terminator angles, respectively. The solar terminator angle is given by $\varepsilon = 23 \cdot 5^0 \sin\left(\frac{\pi(D-81)}{182 \cdot 5}\right)$, where D is the Julian day. Therefore, the maximum drift velocity obtained during November in the Atlantic longitudinal sector (-70 to 0^o) can be explained by the combined effect of enhanced zonal neutral wind speed, minimum geomagnetic field strength, and the alignment of geomagnetic field lines with the solar terminator.

5. Conclusion

In the current study, the evening time zonal neutral wind speed observations from the GOCE satellite and the ion density and vertical drift velocity observations from the C/NOFS satellite are analyzed to investigate the effect of monthly and longitudinal variations of the zonal neutral wind speed on the longitudinal variations of the post-sunset drift velocity of plasma and the associated equatorial ionospheric irregularity. In addition, the relationship of the longitudinal variation of the geomagnetic field strength at the magnetic equator, alignment between the solar terminator and geomagnetic field lines, and the Pedersen conductivity of the ionosphere on the longitudinal variations of vertical drift and ion irregularity are investigated. Based on the analysis presented, the following conclusions have been drawn.

- The seasonal asymmetry of occurrence of irregularities correlates with the seasonal asymmetry of the vertical drift velocity and eastward zonal wind speed.
- At most 50.85% of the longitudinal variations of the equatorial ionospheric plasma vertical drift velocity is accounted for by the longitudinal variation of the eastward zonal neutral wind speed near the magnetic dip equator only within a particular month.
- When the zonal neutral wind speed magnitude is high, i.e. above 150 m/s, up to 69.20% of the longitudinal variations of the vertical drift velocity is explained by the longitudinal variations of zonal neutral wind speed, geomagnetic field strength, and Pedersen conductivity.
- In Atlantic, Africa, and India sectors, eastward zonal neutral wind speed controls much better the monthly variation than the longitudinal variations of the vertical drift. Corresponding to the correlation coefficient above 0.6529, about 42.63% to 79.80% of the monthly variations of the vertical drift velocity are accounted for by the monthly variations of the neutral wind speed.
- The highest occurrence of irregularity obtained in the Atlantic longitudinal sector during November and December is due to a combined effect of the highest zonal neutral wind speeds, the smallest geomagnetic field strength, and the alignment of geomagnetic field lines and solar terminator.
- Downward vertical drift velocity of plasma is obtained during June solstices that correspond to small eastward zonal neutral wind speed. This relationship might be due to the dominance of Hall current divergence mechanism over the curl-free mechanism in generating the west ward directed PRE after sunse**t**.

Acknowledgment

This work is supported by the Air Force Office of Scientific Research and Air Force Material Command USAF under Award FA9550-16-1-0070. M. Nigussie is grateful to the University of Michigan African Presidential Scholarship (UMAPS) Program, University of Michigan,and ICTP through associate program for the support and hospitality in doing part of the paper. M. B.Moldwin was partially supported by NSF grants AGS 1654044 and AGS-1450512.

CINDI data are provided through the auspices of the CINDI team at the University of Texas at Dallas supported by NASA grant NAS5-01068 (https://cdaweb.gsfc.nasa.gov/cgi-bin/eval1.cgi), the authors thank the CINDI investigator team. Also, the authors thank GOCE (http://eo-virtual-archive1.esa.int/GOCE-Thermosphere.html) satellite team for providing neutral wind speed at the F layer. Also, we thank IRI-2016, NRLMSISE-00, IGRF model developers for using the models to compute necessary ionospheric, thermospheric, and geomagnetic field parameters that have been used for Pedersen conductivity estimation.

References

Anderson, D. N., G. Haerendel (1979), the motion of depleted plasma regions in the equatorial ionopshere, J. Geophys. Res., 84,A8.

Booker, H. G., and Wells, H. W. (1938). Scattering of radio waves by the F-region of the ionosphere. Terr. Magn. Atmos. Elec., 43(3), 249–256. https://doi.org/10.1029/TE043i003p00249

Burke W. J., C. Y. Huang, L. C. Gentile, L. Bauer, (2004a), Seasonal-longitudinal variability of equatorial plasma bubbles, Annales Geophysicae, 22, 3089-3098.

Burke W. J., L. C. Gentile, C. Y. Huang, C. E. Valladares, S. Y. Su, (2004b), Longitudinalvariability of equatorial plasma bubbles observed by DMSP and ROCSAT-1, J. Geophys. Res., 109, A12301, doi:10.1029/2004JA010583.

de La Beaujardiere, O., L. Jeong, B. Basu, S. Basu, T. Beach, P. Bernhardt, W. Burke, K. Groves, R. Heelis, R. Holzworth, C. Huang, D. Hunton, M. Kelley, R. Pfaff, J. Retterer, F. Rich, M. Starks, P. Straus, C. Valladares, (2004), C/NOFS: a mission to forecast scintillations, J. Atmos. Sol. Terr. Phys. 66, 1573-1591.

Doornbos, E., S. Bruinsma, B. Fritsche, P. Visser, J. Van Den IJssel, J. Teixeira Encarnac¸ao, and M. Kern (2013) AIR DENSITY AND WIND RETRIEVAL USING GOCE DATA, Proc. 'ESA Living Planet Symposium 2013', Edinburgh, UK 9–13 September 2013 (ESA SP 722).

Eccles J. V. (1998), Modeling investigation of the evening prereversal enhancement of the zonal electric field in the equatorial ionosphere, J. Geophys., Res. 103, A11, 709-719.

Eccles, J. V., J. P. St. Maurice, R. W. Shunk, (2015), Mechanism underlying the prereversal enhancement of the vertical plasma drift in the low latitude ionosphere, Journal o Geophysical Research, 120, 4950-4970, doi:10.1002/2014JA020664.

Farley, D. T., E. Bonelli, B. G. Fejer, and M. F. Larsen (1986), The prereversal enhancement of the zonal electric field in the equatorial ionosphere, J. Geophys. Res., 91(A12), 13,723–13,728, doi:10.1029/ JA091iA12p13723.

Fejer B. G., L.Scherliess, E. R. de Paula, (1999) Effects of the vertical plasma drift velocity on the generation and evolution of equatorial spread F, J. Geophys. Res., 104, A9, 859-869.

Fejer, B. G., D. T. Farley, R. F. Woodman, and C. Calderon (1979), Dependence of equatorial F region vertical drifts on season and solar cycle, J. Geophys. Res., 84, 5792.

Gentile, L. C., W. J. Burke, F. J. Rick, (2006), A global climatology for equatorial plasma bubbles in the topside ionosphere, Annales Geophysicae, 24, 163-172.
1851–1854, doi:10.1029/ 2000GL000061.

Heelis, R. A. (2004), Electrodynamics in the low and middle latitude ionosphere: A tutorial, J.Atmos. Sol. Terr. Phys. 66(10), 825-838, doi:10.1016/j.jastp.2004.01.034.

Heelis, R. A., P. C. Kendall, R. J. Moffet, D. W. Windle, and H. Rishbeth (1974), Electric coupling of the E and F regions and its effect on the F region drifts and winds, Planet. Space Sci., 22, 743–756, doi:10.1016/0032-0633(74)90144-5.

Hei, M. A., R. A. Heelis, J. P. McClure (2005), Seasonal and longitudinal variation of large-scale topside equatorial plasma depletions, J. Geophys. Res. 110, A12315, doi:10.1029/2005JA011153.

Huang, C. Y., Burke, W. J., Machuzak, J. S., Gentile, L. C., and Sultan, P. J. (2001): DMSP observations of equatorial plasma bubbles in the topside ionosphere near solar maximum, J. Geophys. Res., 106, 8131, 2001.

Huang, C.-S., and M. R. Hairston (2015), The postsunset vertical plasma drift and its effects on the generation of equatorial plasma bubbles observed by the C/NOFS satellite, J. Geophys. Res. Space Physics, 120, 2263–2275, doi:10.1002/2014JA020735.

Huang, C.-S., O.de La Beaujardiere, P. A. Roddy, D. E. Hunton, J. Y. Liu, and S. P. Chen, (2014) occurrence probability and amplitude of equatorial ionospheric irregularities associated with

plasma bubbles during low and moderate solar activity (2008-2012), J.Geophys. Res., 119, 1186-1199,doi:10.1002/2013JA019212.

Kil, H., L. J. Paxton, and S.-J. Oh (2009) Global bubble distribution seen from ROCSAT-1 and its association with the evening prereversal enhancement, J. Geophys. Res., 114, A06307, doi:10.1029/2008JA013672.

Liu, H., E. Doornbos, and J. Nakashima (2016) Thermospheric wind observed by GOCE: Wind jets and seasonal variations, J. Geophys. Res. Space Physics, 121, 6901–6913, doi:10.1002/2016JA022938.

Maute A., A. D. Richmond, R. G. Roble, Sources of low-latitude ionospheric ExB and their variability, J. Geophys. Res., 117, A06312, doi:10.1029/2011JA017502.

Ott, E. (1978) Theory of Rayleigh-Taylor bubbles in the equatorial ionosphere, J. Geophys. Res., 83, 2066.

Ren, Z., W. Wan, L. Liu, R. A. Heelis, B. Zhao, Y. Wei, and X. Yue (2009), Influences of geomagnetic fields on longitudinal variations of vertical plasma drifts in the presunset equatorial topside ionosphere, J. Geophys. Res., 114, A03305, doi:10.1029/2008JA013675.

Richmond, A. D., A. Maute (2014). Ionospheric electrodynamics modeling. In J. Huba, R. Schunk, & G. Khazanov (Eds.), *Modeling the Ionosphere-Thermosphere System* (pp. 57-73). Washington: American Geophysical Union. doi:10.1002/9781118704417.ch6

Rishbeth, H. (1971), The F-layer dynamo, Planet. Space Sci., 19, 263–267, doi:10.1016/0032 0633(71)90205-4.

Paznukhov V. V., C. S. Carrano, P. H. Doherty, K. M. Groves, R. G. Caton, C. E. Valladares, G. K. Seemala, C. T. Bridgwood, J. Adeniyi, L. L. N. Amaeshi, B. Damtie, F. D'UjangaMutonyi, J. O. Ndeda, P. Baki, O. K. Obrou, B. Okere, G. M. Tsidu, (2012), Equatorial plasma bubbles and L-band scintillation in Africa during solar minimum, Ann. Geophys., 30, 675-682.

Tsunoda, R. T. (2010), On seeding equatorial spread F during solstices, Geophys. Res. Lett., 37, L05102, doi:10.1029/2010GL042576.

Tsunoda, R. T. (1985), Control of the seasonal and longitudinal occurrence of equatorial scintillation by the longitudinal gradient of in integrated E region conductivity, J. Geophys. Res., 90, 447-456.

Shunk, R., A. Nagy (2009), Ionospheres, physics, plasma physics, and chemistry, second edition.

Su, S.-Y., C. K. Chao, and C. H. Liu (2006), On monthly/seasonal/longitudinal variations of equatorial irregularity occurrences and their relationship with the post-sunset vertical drift velocities, J. Geophys. Res., 113, A05307, doi:10.1029/2007JA012809

Sultan, P. J. (1996), Linear theory and modeling of the Rayleigh-Taylor instability leading to the occurrence of equatorial spread F, J. Geophys. Res., 101, A12, 875-891.

Vichare G., A. D. Richmond (2005), Simulation study of the longitudinal variation of eveing vertical ionospheric drifts at the magnetic equator during equinox, J. Geophys. Res., 110, A05304, doi:10.1029/2004JA010720.

Yizengaw E., P. Doherty, T. Fuller-Rowell (2013) Is Space Weather Different Over Africa, and If So, Why? An AGU Chapman Conference Report, Space Weather, 11, 389–391, doi:10.1002/swe.20063, 2013

Zhang S. R., J. C. Foster, J. M. Molt, P. J. Erickson, A. J. Coster (2012) Magnetic declination and zonal wind effects on longitudinal differences of ionospheric electron density at mid latitudes, J. Geophys. Res. 117, A08329,doi:10.1029/2012JA017954.

Figures caption:

Figure 1: sample ion density deviations (top panels), maximum drift velocity (middle panels), and zonal wind speed on selected days shown as title of each panel.

Figure 2: distribution of zonal neutral wind speed obtained just at the magnetic equator over the globe for the months of year 2011.

Figure 3: distribution of zonal neutral wind speed obtained just at the magnetic equator over the globe for the months of year 2012.

Figure 4: map of ion density perturbation occurrence (1^{st}, 2^{nd} columns for different ion density irregularity thresholds), maximum vertical drift velocity (3^{th} column), and zonal wind speed (4^{th} panels) versus longitude and month for the years 2011 (top panels) and 2012 (bottom panels).

Figure 5: longitudinal scatter plot of drift velocity versus zonal wind speed obtained by averaging for every 30^{o} bin of longitude for each month of the year 2011.

Figure 6: longitudinal scatter plot of drift velocity versus zonal wind speed obtained by averaging for every 30^{o} bin of longitude for each month of the year 2012.

Figure 7: longitudinal scatter plot of drift velocity versus zonal wind speed obtained by averaging for every 30^o bin of longitude for each season of the years 2011 (top panels) and 2012 (bottom panels).

Figure 8: longitudinal variation of vertical drift velocity, zonal neutral wind, and geomagnetic field strength at magnetic equator, and field-line integrated Pederson conductivity (Σ_p), from top to bottom, for March (left) and November (right) 2011.

Figure 9: longitudinal variation of vertical drift velocity, zonal neutral wind, and geomagnetic field strength at magnetic equator, and field-line integrated Pederson conductivity (Σ_p), from top to bottom, for March (left) and November (right) 2012.

Figure 10: monthly scatter plot of drift velocity versus zonal wind speed obtained for every 30^o longitude bins for the year 2011.

Figure 11: monthly scatter plot of drift velocity versus zonal wind speed obtained for every 30^o longitude bins for the year 2012.

Figure 12: Days of the year (DOY) when the angle between the geomagnetic field lines and solar terminator approximately zero over the globe.

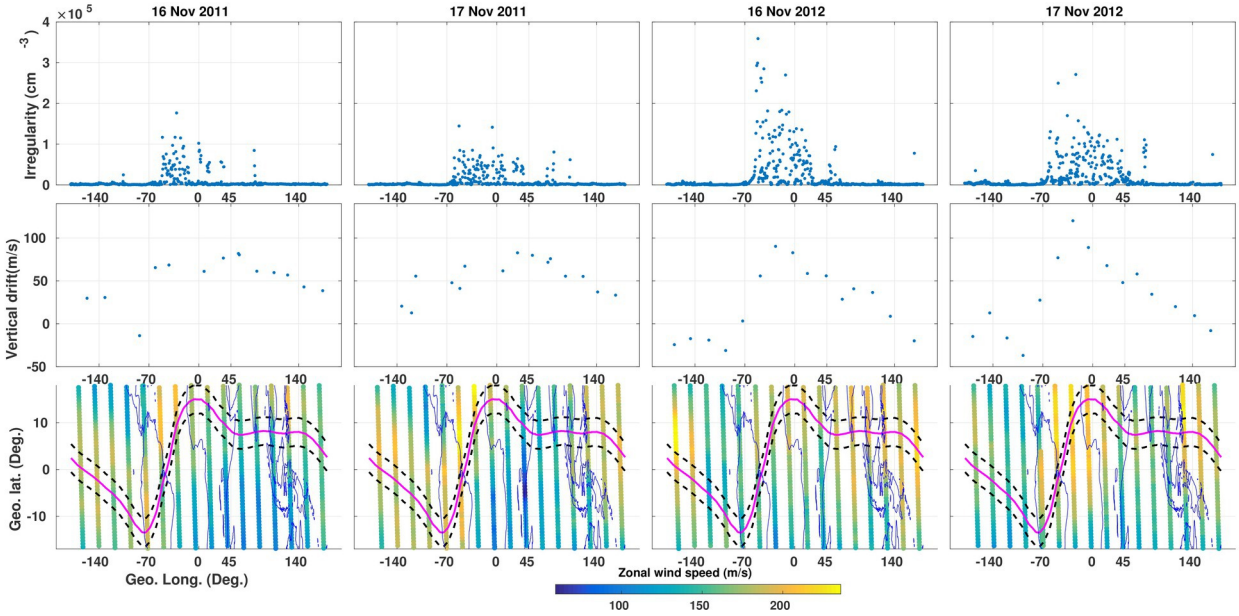

2019ja027671-f01-z-.eps

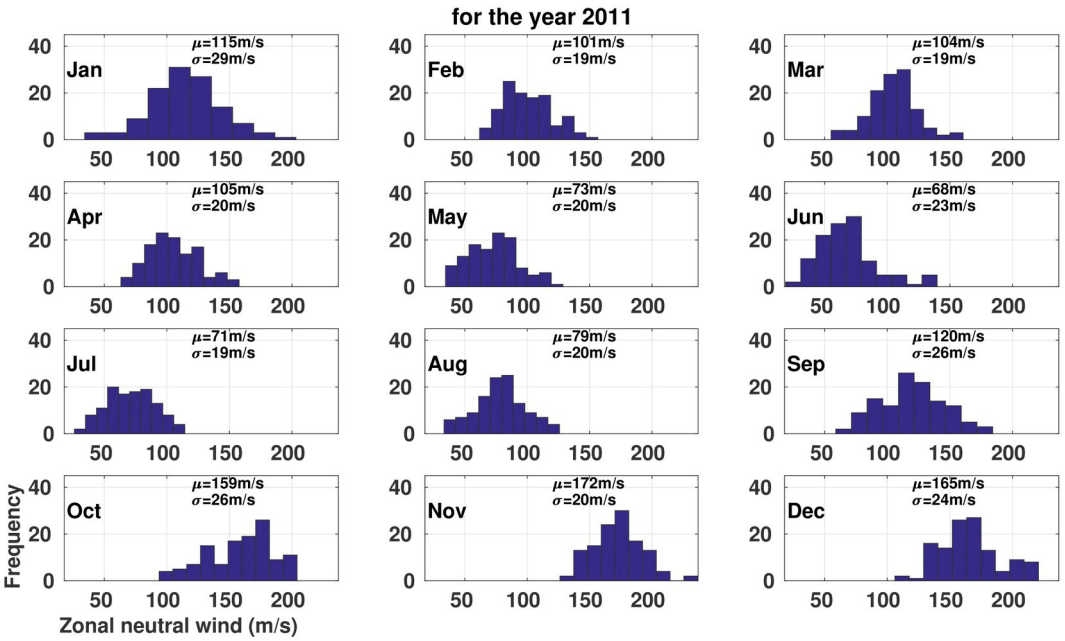

2019ja027671-f02-z-.eps

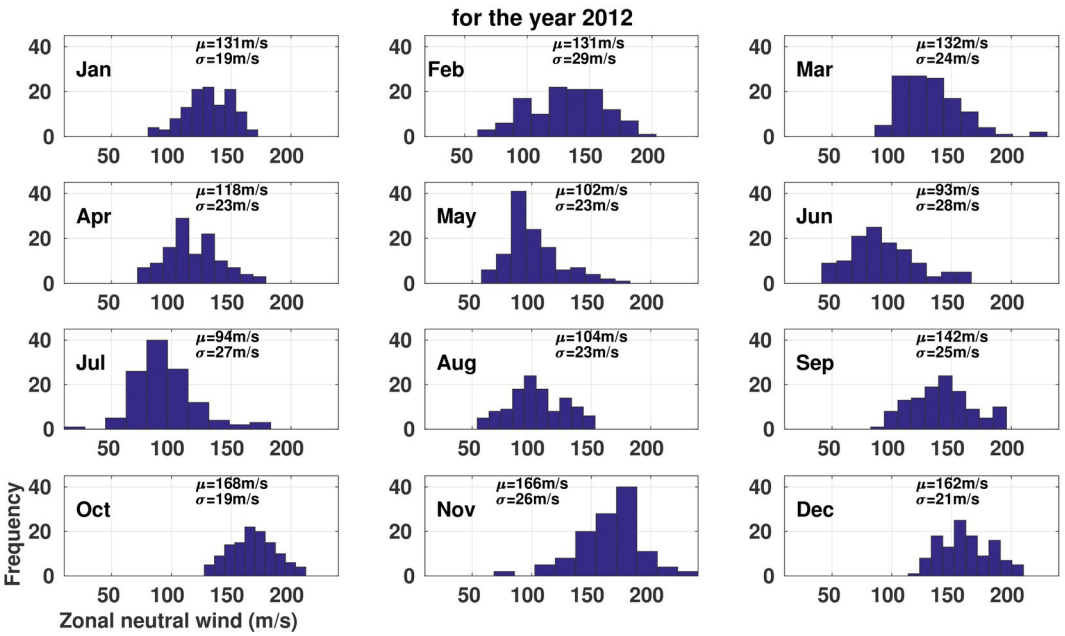

2019ja027671-f03-z-.eps

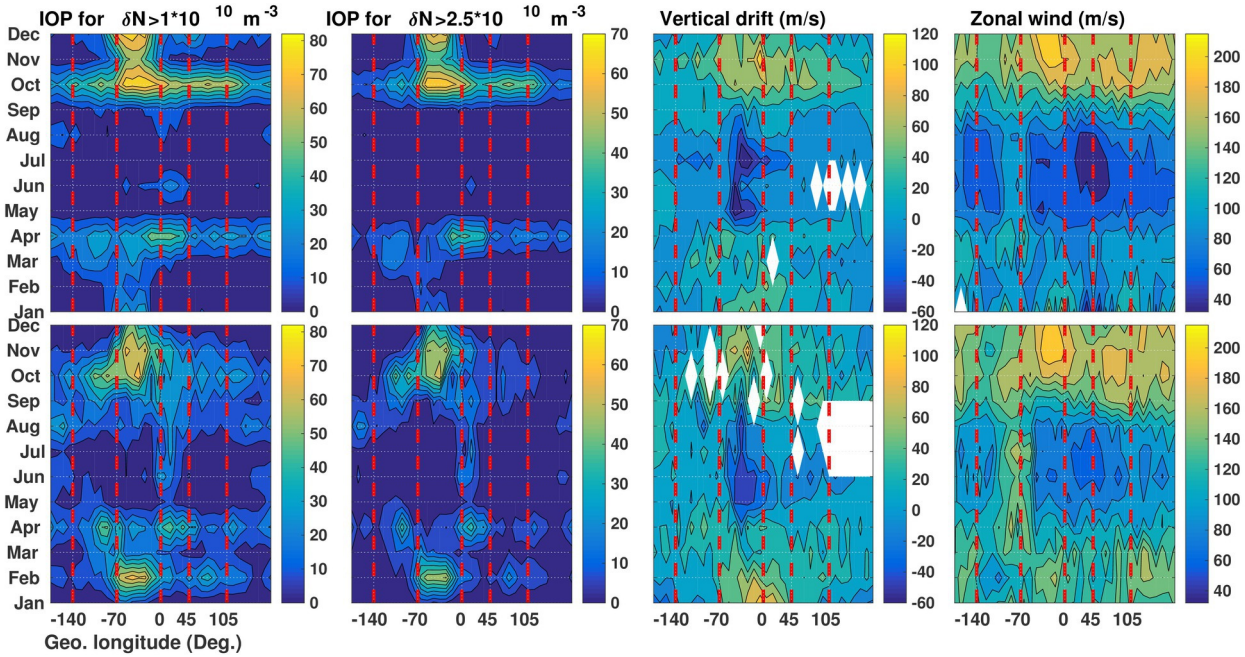

2019ja027671-f04-z-.eps

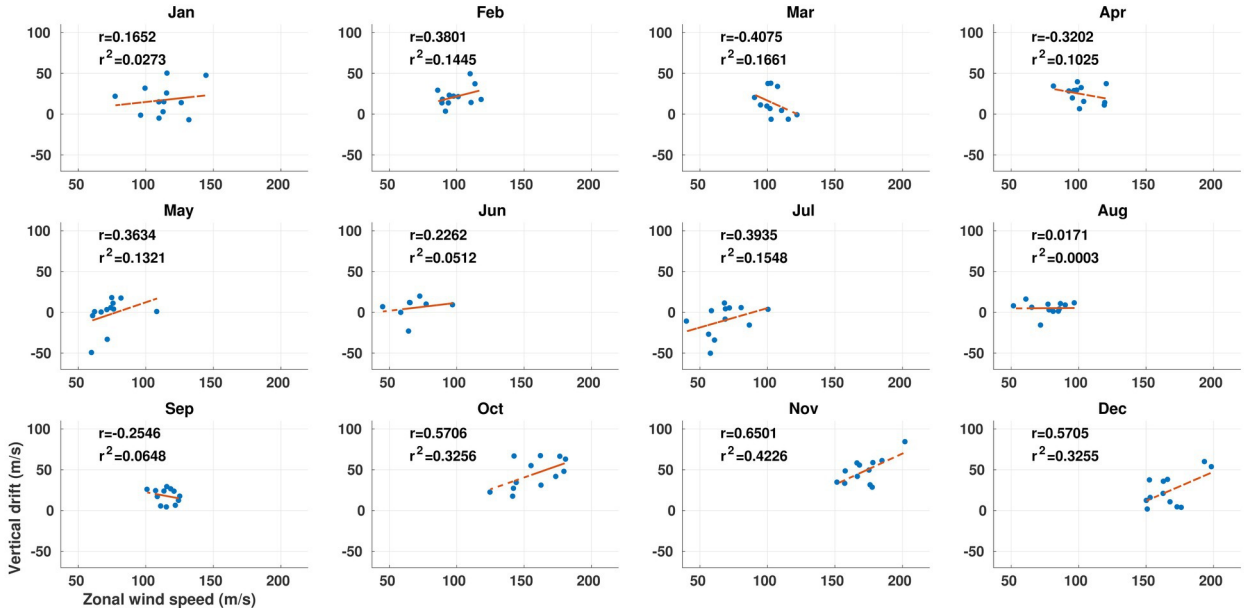

2019ja027671-f05-z-.eps

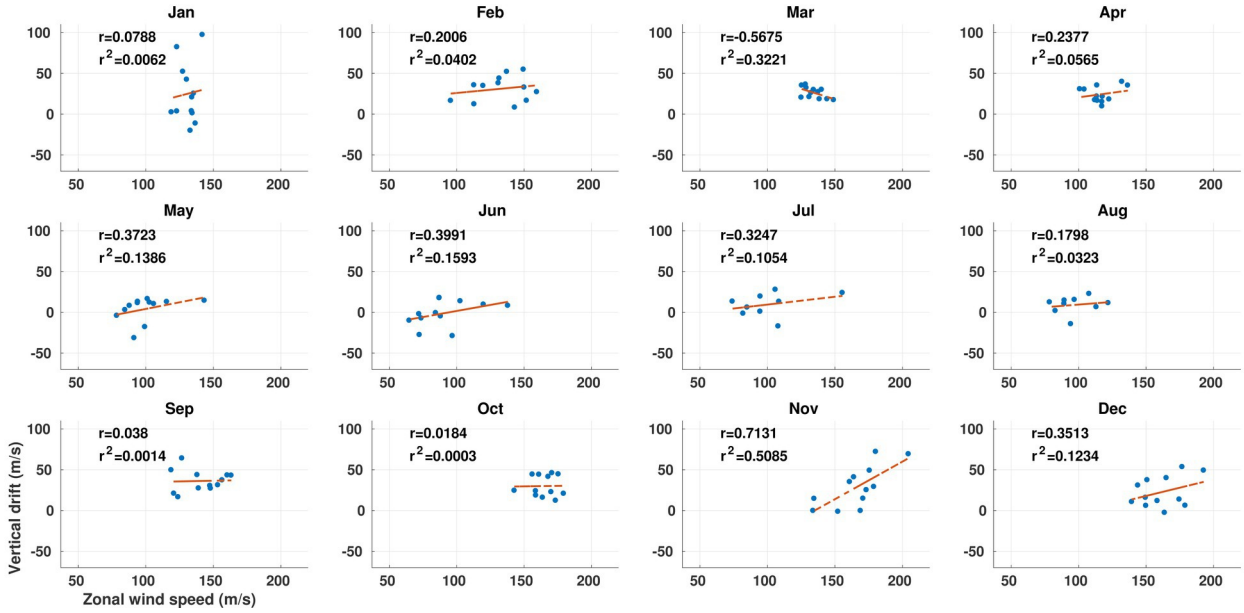

2019ja027671-f06-z-.eps

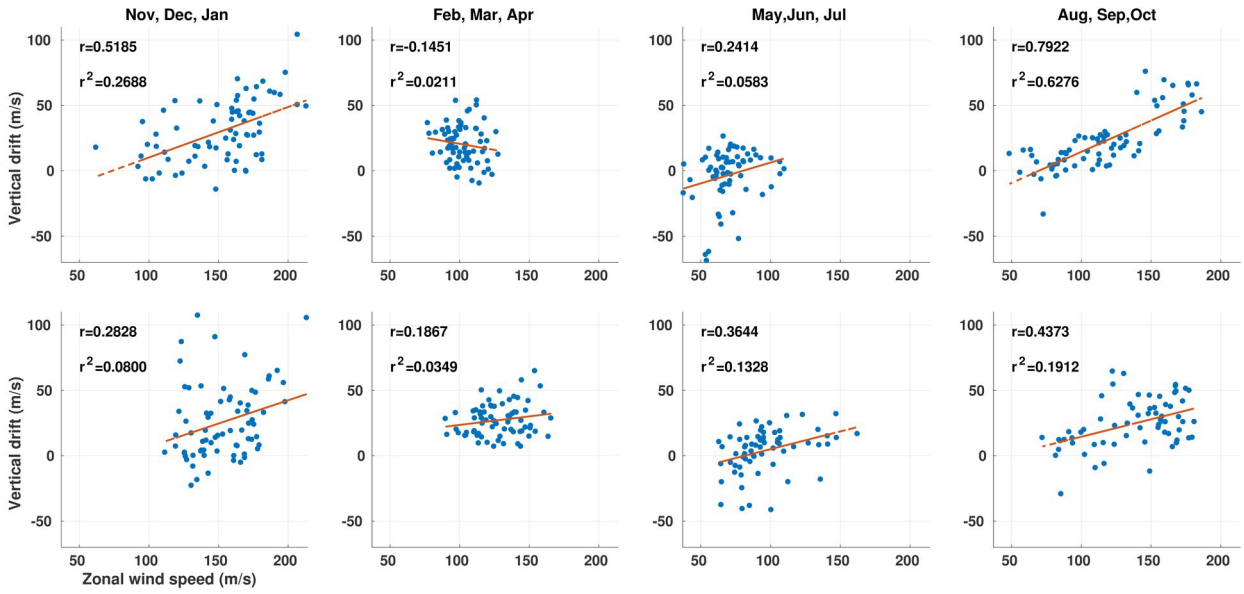

2019ja027671-f07-z-.eps

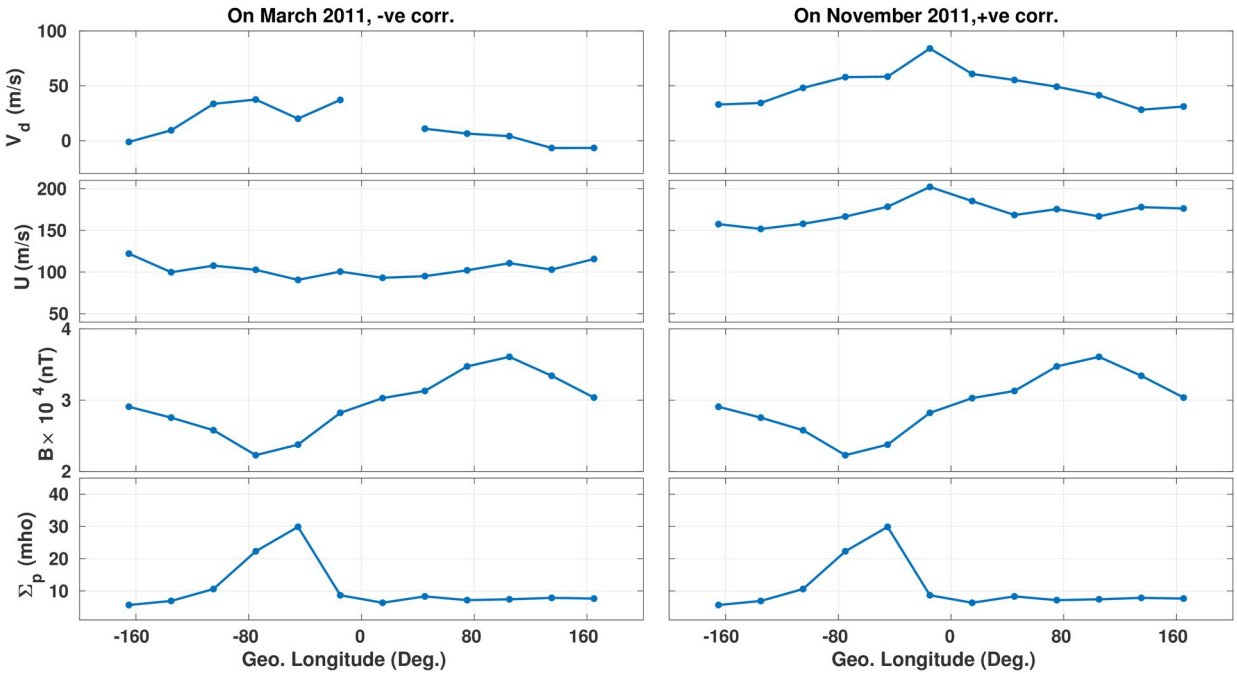

2019ja027671-f08-z-.eps

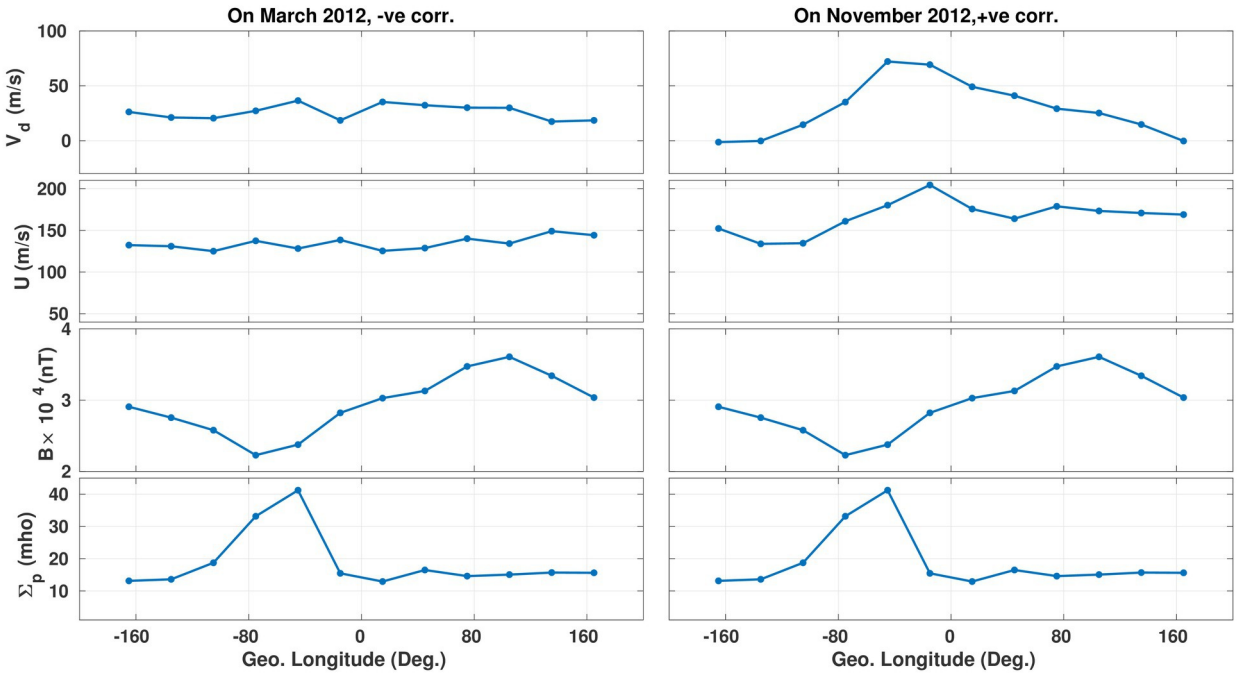

2019ja027671-f09-z-.eps

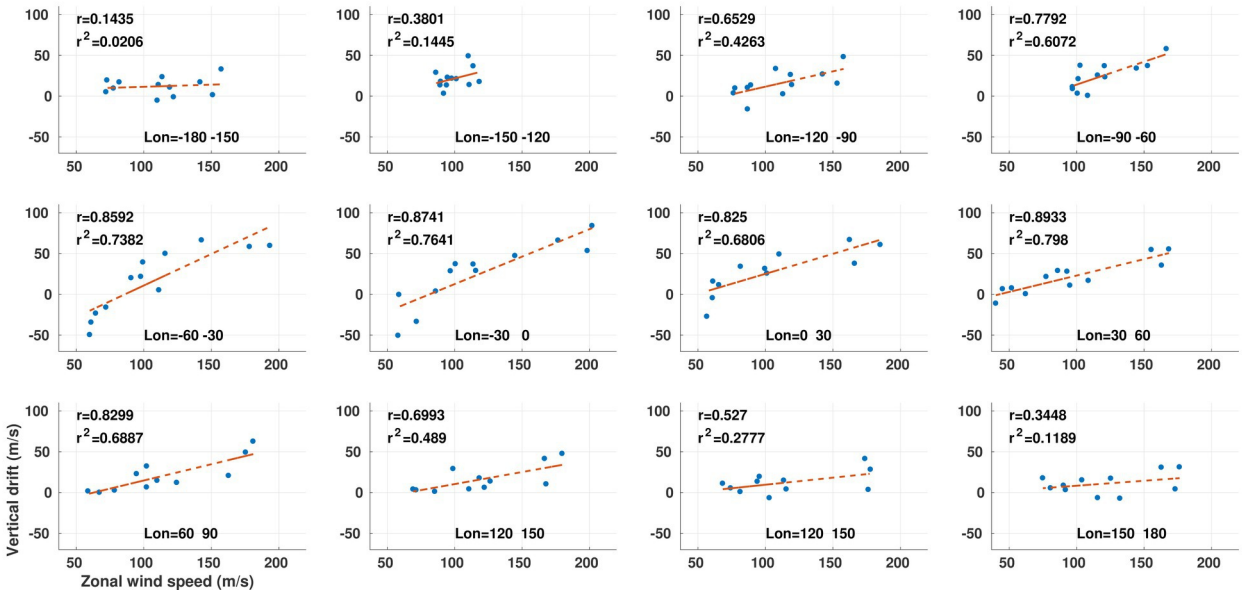

2019ja027671-f10-z-.eps

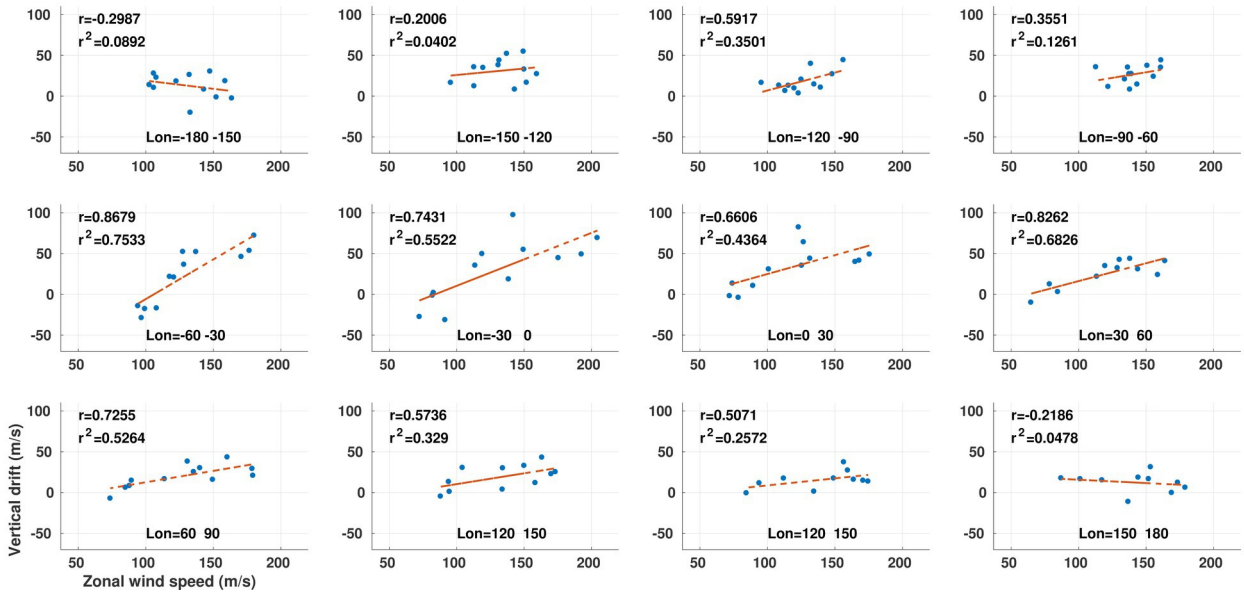

2019ja027671-f11-z-.eps

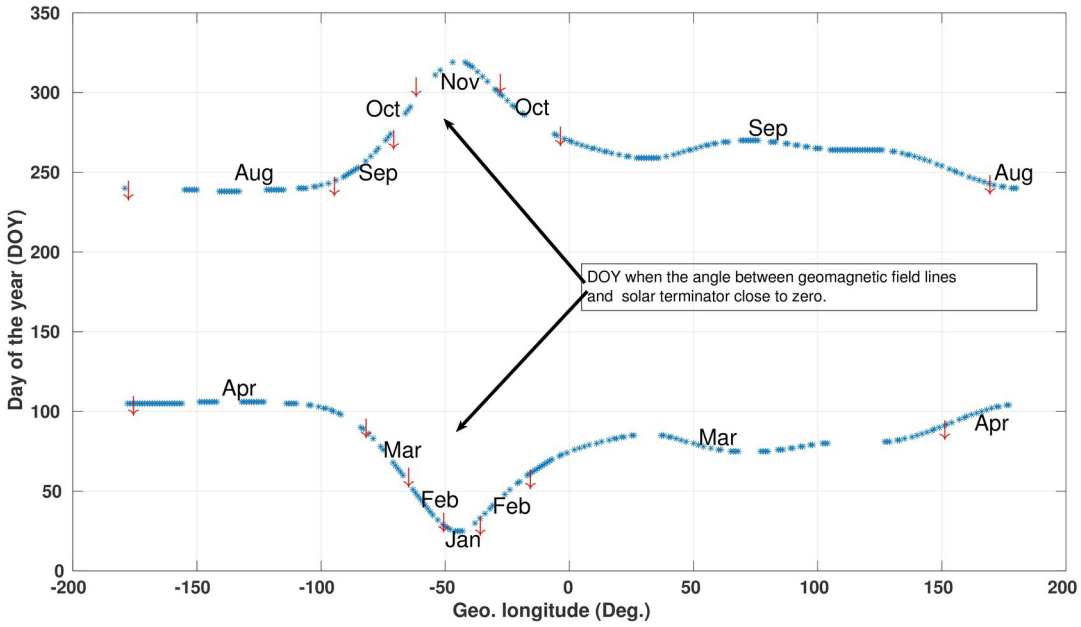

2019ja027671-f12-z-.eps